Bulletin of the Seismological Society of America, Vol. 96, No. 4B, pp. S143–S158, September 2006, doi: 10.1785/0120050826

Ⓔ

Kinematic Inversion of the 2004 **M** 6.0 Parkfield Earthquake Including an Approximation to Site Effects

by Pengcheng Liu, Susana Custódio, and Ralph J. Archuleta

Abstract The 2004 **M** 6.0 Parkfield earthquake yielded one of the largest amounts of near-source strong ground motion seismic data ever. We invert strong-motion seismograms to obtain a model for the space–time distribution of coseismic slip on the fault. To reduce noise in the inversion, we take into account local amplifications that affect each station by using records of the 1983 **M** 6.5 Coalinga earthquake. Site amplification correlates well with large peak ground velocities registered during the 2004 Parkfield mainshock. The inversion for a kinematic rupture model yields a nonunique solution; we therefore analyze various rupture models that explain the data equally well. Our preferred rupture model identifies a primary zone of high slip surrounding the hypocenter, where the maximum slip is 57 cm. A secondary slip area, over which contours are not well resolved, is located northwest of the hypocenter. The rupture speed is highly heterogeneous. We infer an average rupture velocity of ~2.8 km/sec close to the hypocenter, and of ~3.3 km/sec in the secondary region of large slip to the northwest of the hypocenter. By correlation of our rupture model with both microseismicity and velocity structure, we identify six patches on the fault plane that behave in seismically distinct ways.

Online material: Kinematic rupture model parameters.

Introduction

An earthquake is the manifestation of sudden slip along a fault plane, an event that radiates energy in the form of elastic waves. The study of earthquake physics is constrained by the inability to measure coseismic slip everywhere on the fault during the rupture process. In order to understand the seismic source, one must rely on ground motion recorded at a given distance from the fault. However, seismograms carry information not only about the rupture process, but also about the material traversed by the waves from the source to the observation point—path effects. In addition, seismograms capture reverberations and nonlinear effects close to the surface—site effects. Isolating the desired rupture information in the seismic records is a nontrivial task. In the study of earthquake dynamics, a controlled experimental event, on a real Earth scale, cannot be achieved. With the time of occurrence and the location of earthquakes unknown beforehand, data that document a large event are difficult to obtain. Quality data sets are therefore invaluable.

The idea of trapping, that is, densely recording an earthquake, with geophysical instruments, became a reality in the Parkfield section of the San Andreas Fault, California (Bakun *et al.*, 2005). The analysis of seismic data from prior **M** 6.0 Parkfield events led Bakun and McEvilly (1984) to predict that another **M** 6.0 earthquake was due in Parkfield between 1983 and 1993. Bakun and Lindh (1985) furthermore proposed the concept of characteristic earthquakes—seismic events with persisting features. The characteristic Parkfield earthquake would occur about every 22 years, nucleate at a common hypocenter, and grow into a **M** 6.0 event by rupturing the same fault area, from northwest to southeast. Their work led to the Parkfield Prediction Experiment (Bakun and Lindh, 1985; Roeloffs and Langbein, 1994), a large-scale project designed to record a complete earthquake cycle of preseismic, coseismic, and postseismic periods. In the years after the prediction, Parkfield became one of the most intensely studied fault zones in the world (e.g., Ben Zion *et al.*, 1993; Eberhart-Phillips and Michael, 1993; Fletcher and Spudich, 1998; Harris and Segall, 1987; Li *et al.*, 1990, 2004; *Malin and Alvarez*, 1992; Michelini and McEvilly, 1991; Murray *et al.*, 2001; Segall and Du, 1993; Thurber *et al.*, 2003; Unsworth and Bedrosian, 2004; Waldhauser *et al.* 2004).

The most recent **M** 6.0 Parkfield earthquake occurred on 28 September 2004 (Bakun *et al.*, 2005). A data set of unprecedented quantity, quality, and diversity was generated during the event. Preliminary analysis (Langbein *et al.*, 2005) reveals that the 2004 rupture, unlike previous **M** 6 Parkfield earthquakes, propagated from southeast to northwest. Although the fault area that broke in 2004 is coincident with previous ruptures, the hypocenter itself was 20 km southeast of the 1922, 1934, and 1966 hypocenters (Fig. 1). Very large peak ground accelerations (PGA's) and peak ground velocities (PGV's) were observed at both ends of the slip area (Shakal *et al.*, 2006). No surface fracture appeared at the time of the earthquake, but surface afterslip began 1–24 hr after the mainshock (Rymer *et al.*, 2006). Aftershocks extended for ~40 km along the fault, in a pattern that overlaps previous microseismicity (Thurber *et al.*, 2006).

In this article we initiate a study of the 2004 Parkfield mainshock rupture. We derive a kinematic model for coseismic slip on the fault from inversion of strong-motion, near-fault seismograms. Rather than finding a single model, we compute 10 rupture models that fit the data equally well. A statistical study of the models indicates which areas of the fault have well-resolved parameters. To account for local geological conditions, we estimate site effects on the Parkfield array. Those site effects are inferred from seismic records of the 1983 Coalinga earthquake and were included in our inversions through a weighting scheme and an amplitude correction. Finally, we compare the kinematic rupture model to microseismicity and to velocity structure.

Data

Our study uses acceleration records from 43 three-component strong-motion instruments (Fig. 1, Table 1). Of the 43 instruments, 33 are analog recorders operated by the California Geological Survey (CGS) network (McJunkin and Shakal, 1983; Shakal *et al.*, 2006). The remaining 10 are digital recorders maintained by the United States Geological Survey (USGS) (Borcherdt *et al.*, 2004). The choice of stations was based on the following criteria:

- Proximity to epicenter must be less than 32 km
- Instrumental frequency response must be flat above 0.16 Hz
- Seismograms must display clear *S* arrivals.

The acceleration records were integrated into velocity waveforms and then filtered in a passband of 0.16–1.0 Hz with a zero-phase (forward and backward) butterworth 4-pole filter. The lower limit of frequencies to be used in the inversion is dictated by instrument capability—below 0.16 Hz most of these strong-motion seismograms are inaccurate. The upper frequency limit is determined by the band of applicability of the Green's functions, which in turn depends on the grid spacing at which the velocity structure is known. We do not use the absolute time of the seismic records. Instead, we align the recorded *S* arrival at each station with the theoretical *S*-arrival time as predicted from the velocity structure. This procedure renders the inversion more stable and accurate as it reduces the effect of errors inherent to the velocity structure.

In our study we did not use the fault-parallel motion recorded at stations CH2W, FZ1, and GH1W because the first pulse recorded at these stations was opposite to what expected from the relative position of the station with respect to the fault plane. This disagreement is probably due to our oversimplification of the fault geometry (a plane is assumed) or to velocity structure complexities. For all other stations, the three waveforms recorded by each instrument (two horizontal components and one vertical) were used in the inversion; but not all data were weighted equally. The San-Andreas Fault accommodates primarily right-lateral motion between the Pacific plate and the North American plate (Wallace, 1990). In the Parkfield area, earthquake motion is dominantly strike-slip (Thurber *et al.*, 2006). Consequently, the horizontal components record the most significant ground motion and display a higher signal-to-noise ratio than the vertical records do. In the inversion, vertical waveforms were down weighted by a factor of 10 relative to the two horizontals. Each station was given a weight based on its local geological condition. Stations that showed resonances in the passband 0.16–1.0 Hz were given low weights, while those that record clean source signals were given high weights.

Site Amplifications and Resonances Inferred from the Coalinga Earthquake

Assessment of site effects was based on data recorded at the Parkfield array during the 1983 **M** 6.5 Coalinga earthquake. The Coalinga thrust earthquake (strike, 145°; dip, 30° W; rake, 100°) (Eberhart-Phillips, 1989) occurred 25 km northeast of Parkfield, illuminating almost equally all stations in the Parkfield array. Assuming the source is common to all stations, we use the deviation from a reference source spectrum as a measure of the site effect.

We computed spectra for the Coalinga earthquake using the multitaper algorithm, a spectral estimator that produces smoother spectra than those obtained by fast Fourier transform (Kilb *et al.*, 2003). To account for geometrical spreading—decay of the amplitude of seismic waves with distance from the source—spectra were multiplied by the hypocentral distance. Figure 2 shows spectra for both horizontal components for all Parkfield stations that recorded the Coalinga earthquake. The digital USGS stations were not installed at the time. We took the median of the horizontal spectra recorded at the six stations with lowest amplitude spectra in the frequency range of interest to our inversion (0.16 Hz $< f <$ 1 Hz)—VC4W, VC2W, CH5W, SC1E, CH2E, and CH4A—as the reference source spectrum for the Coalinga earthquake. We expect this reference source spectrum to provide a good estimation of the ground motion that would be recorded at a rock site during the Coalinga earthquake. We prefer to use the median rather than the average because the median is less sensitive to outliers. For each station, we compared the average of the two horizontal spectra (referred to here as horizontal spectrum) to the source spectrum. The site ratio SR (Fig. 3), which is found by dividing the horizontal

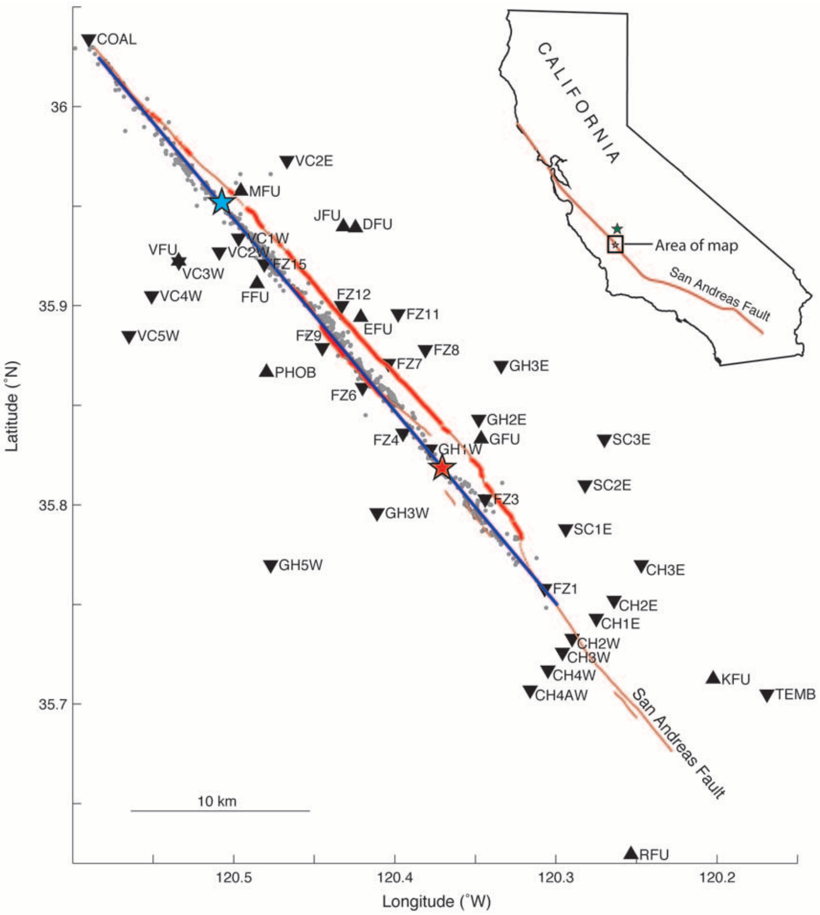

Figure 1. Map of the Parkfield segment of the San Andreas Fault. Stations used in the inversion are represented by the following: normal triangles, USGS stations; inverted triangles, CGS stations. Red star, 2004 Parkfield epicenter; Light blue star, 1992, 1934, and 1966 colocated epicenters; blue line, modeled fault profile; gray dots, aftershocks located by Thurber *et al.* (2006). Also shown is the San Ańdreas Fault trace (brown) and regions where postseismic surface slip occurred (red) as mapped by Rymer *et al.* (2006). The inset map of California shows the locations of the 2004 Parkfield epicenter (red star) and 1983 Coalinga epicenter (green star).

spectrum at each station by the source spectrum (the median of the six stations mentioned above), provides two types of information:

1. Local amplification. Ground motion is amplified relative to the source signal when the amplitude of the horizontal spectra is consistently larger than the amplitude of the source spectrum. In this case, SR > 1 at all frequencies. The amplification factor A_i at station i is given by $A_i =$ SR, where SR is the average of the site ratio over the frequency band 0.16–1.0 Hz.
2. Resonance. Peaks in SR reveal the amplification of specific frequencies. The variance of the site ratio *var(SR)* is large in the presence of strong spectral peaks; the larger *var(SR),* the stronger the resonance. The weight W_i given to station i in the inversion is inversely proportional to *var(SR)* (computed in the band 0.16–1.0 Hz). We limit W_i so that $\frac{1}{m} < W_i < m$. If a large m-value is chosen, more weight is given to stations with flat spectra in the frequency range of interest. In such a case, stations with a higher signal-to-noise ratio, which are more easily fit in the inversion, play a more important role in deriving the rupture model. Therefore, larger m-values lead to lower overall numerical misfits in the inversions. On the other hand, if a too large m-value is used, stations more affected by site effects play almost no role in the inversion. In order to prevent large weight differences between stations, we use $m = 2$. Thus, in our calculations, the station with the most flat SR is assigned a weight four times that of the station with largest spectral variation. We performed inversions for different values of m; whereas the overall misfit of the inversion goes down systematically as m increases, the gross features of the final rupture models remain similar.

In this manner, the site ratio SR yields the degree of ground-motion amplification at each station and sets the weight that it is assigned in the inversion (Table 2). In the absence of information on the site effects at stations that were not installed at the time of the Coalinga earthquake but that were used in the inversion, we were forced to assume values for the amplification factor and weight at those stations. We assumed $A_i = 1$ and $W_i = 1.5$, values that agree with what would be expected from the stations locations (Fig. 4). We also computed inversions assuming that $W_i = 1$ at such stations, which resulted in final rupture models similar to the ones obtained assuming $W_i = 1.5$. That is, the inversion is not very sensitive to these values, probably due to the large amount of data inverted and consequent redundancy of information.

Table 1
List of Strong-Motion Seismic Stations Used in the Inversion

Station	Latitude (°N)	Longitude (°W)	Digital	Analog
C1E	35.743	120.275		X
CH2E	35.752	120.264		X
CH2W	35.733	120.290		X
CH3E	35.770	120.247		X
CH3W	35.726	120.296		X
CH4AW	35.707	120.316		X
CH4W	35.717	120.305		X
COAL	36.034	120.590		X
DFU	35.939	120.424	X	
EFU	35.894	120.421	X	
FFU	35.911	120.486	X	
FZ1	35.758	120.307		X
FZ3	35.803	120.344		X
FZ4	35.836	120.395		X
FZ6	35.859	120.420		X
FZ7	35.871	120.404		X
FZ8	35.878	120.381		X
FZ9	35.879	120.445		X
FZ11	35.896	120.398		X
FZ12	35.900	120.433		X
FZ15	35.921	120.481		X
GFU	35.833	120.346	X	
GH1W	35.828	120.378		X
GH2E	35.843	120.348		X
GH3E	35.870	120.334		X
GH3W	35.796	120.411		X
GH5W	35.770	120.477		X
JFU	35.940	120.432	X	
KFU	35.713	120.203	X	
MFU	35.958	120.496	X	
PHOB	35.867	120.480	X	
SC1E	35.788	120.294		X
SC2E	35.810	120.282		X
SC3E	35.833	120.270		X
RFU	35.624	120.254	X	
TEMB	35.705	120.169		X
VC1W	35.934	120.497		X
VC2E	35.973	120.467		X
VC2W	35.927	120.509		X
VC3W	35.922	120.534		X
VC4W	35.905	120.551		X
VC5W	35.885	120.565		X
VFU	35.923	120.534	X	

Station location and instrument type is also indicated.

The strongest amplification and resonances occur for stations close to the fault zone (Fig. 4)—an observation consistent with three-dimensional (3D) velocity profiles of Parkfield. The 3D structural models (Michelini and McEvilly, 1991; Eberhart-Phillips and Michael, 1993; Thurber *et al.*, 2003) and trapped waves studies (Li *et al.*, 2004) show low-velocity regions on the fault zone that would amplify seismic waves. A magnetotelluric study reveals a low-resistivity body on the fault zone (Unsworth and Bedrosian, 2004). This fault-zone conductor is interpreted as fractured rock with a high percentage of pore fluids.

Kinematic Inversion

In the search for a proper rupture model, we invert velocity waveforms to find the temporal and spatial distribution of coseismic slip on the fault using the method of Liu and Archuleta (2004). The result is a kinematic model characterized by five source parameters: slip amplitude (magnitude of slip), slip rake (direction of slip), rupture velocity (related to rupture time—the average time between rupture onset at the hypocenter and rupture arrival at a given point on the fault), and an accelerating and decelerating rise time (the two combined give the duration of slip). The task of finding a source model that best fits the observed data can be divided into two smaller problems: forward and inverse. The forward problem consists of generating waveforms at the surface based on a particular rupture model. The inverse problem requires minimizing the difference between observed waveforms and synthetics generated by various source models.

Forward Problem

Source parameters are determined on a 2 km $\times$ 2 km grid (Fig. 5A). We assume that slip rate at each point is described by the function $\dot{s}(t)$ (equation 1) (Fig. 5B).

$$\dot{s}(t) = \begin{cases} A\left[\sin\left(\dfrac{t}{T_1}\dfrac{\pi}{2}\right)\right] & \text{if } 0 < t < T_1 \\ \dfrac{A}{2}\left[1 + \cos\left(\dfrac{t - T_1}{T_2}\pi\right)\right] & \text{if } T_1 < t < T_1 + T_2. \end{cases} \quad (1)$$

$$\text{where} \quad \frac{1}{A} = \frac{2T_1}{\pi} + \frac{T_2}{2}$$

The total rise time T is comprised of an accelerating time T_1 and a decelerating time T_2, such that $T = T_1 + T_2$. The values of T_1 and T_2 are two independent parameters in the inversion. Because the inversion is nonlinear (Liu and Archuleta, 2004), we must set an allowable range for each of the kinematic parameters. The range of values allowed for the source parameters is given in Table 3.

Green's functions are computed on a finer grid (500 m $\times$ 500 m) using the frequency–wavenumber (*f-k*) method of Zhu and Rivera (2002). This method propagates displacement, in the frequency domain, through a multilayered media. The Green's functions calculation takes as input a one-dimensional (1D) bilateral velocity structure, adapted from the 3D models of Thurber *et al.* (2006) and Eberhart-Phillips and Michael (1993). The velocity model we use (Table 4, Fig. 6) takes in account the different materials on the two sides of the fault. The granitic Salinian block, west of the fault, is generally faster than the sedimentary Franciscan terrane, east of the fault.

We interpolate the two components of slip (along-strike and down-dip), slowness (the inverse of rupture velocity),

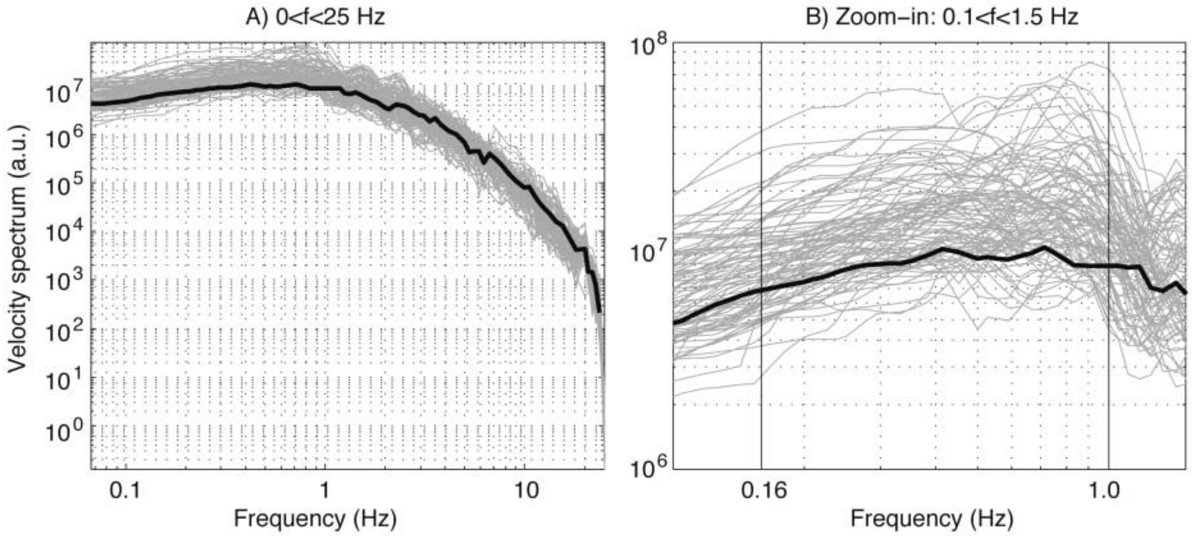

Figure 2. Coalinga earthquake spectra recorded at Parkfield. All spectra were computed using a multitaper algorithm. Gray lines, horizontal component spectra; black thick line, reference source spectrum. (A) Frequency range: 0 Hz $< f <$ 25 Hz. (B) Zoom in at 0.1 Hz $< f <$ 1.5 Hz. The two vertical lines indicate the limits of the frequency band used in the inversion (0.16 Hz $< f <$ 1.0 Hz).

and T_1 and T_2—all directly related to the source parameters we invert for—onto a finer spacing of 167 m $\times$ 167 m. Green's functions also undergo bilinear interpolation onto the same fine spacing. At every node of this finer grid, source parameters are convolved with Green's functions. The resulting waveform is the ground motion generated by slip on the patch surrounding the node. The sum of ground velocities arising from all nodes yields the final synthetic waveform.

We set the geometry of the fault according to the location of aftershocks (Thurber *et al.*, 2006): strike, 140° SE; dip, 87° SW; length, 40 km; width, 15 km. Because no surface break was observed at the time of the mainshock, our fault plane is buried 500 m below the surface. The hypocenter is located at 35.8185° N, 120.3706° W, and at a depth of 8.26 km, in agreement with relocated seismicity (J. Hardebeck, personal comm., 2005).

Inverse Problem

The goal of the inverse problem is to minimize a misfit function $E(M)$ (equation 2) that measures the difference between observed velocity waveforms $\dot{u}_o(t)$ and synthetic velocity waveforms $\dot{u}_s(t)$ generated by a slip model M. We use the misfit function from Spudich and Miller (1990):

$$E(M) = \sum_{d=1}^{N_d} W_d \left(1 - \frac{2\sum_{t_b}^{t_e} \dot{u}_s(t)\, \dfrac{\dot{u}_0(t)}{A_d}}{\sum_{t_b}^{t_e} \dot{u}_S^2(t) + \sum_{t_b}^{t_e} \left(\dfrac{\dot{u}_0(t)}{A_d}\right)^2} \right) + W_C \,(\text{constraints}). \quad (2)$$

Each of the N_d observed waveforms is given a weight W_d and corrected by an amplification factor A_d corresponding to the station i where waveform d was recorded. The misfit function $E(M)$ is scale invariant: consequently, the weight given to each waveform is independent of its absolute amplitude. In order to take into account the lower signal-to-noise ratio of the vertical waveforms, we downweight them. For horizontal data $W_d = W_i$, and for vertical data $W_d = 0.1\,W_i$. The waveform to be inverted $\dot{u}_o(t)\ /\ A_d$ is obtained by dividing the observed velocity record by the amplification factor $A_d = A_i$. We impose two constraints on the rupture model: smoothness and a target seismic moment. W_c dictates how strongly the constraints are imposed. Both the along-strike and down-dip components of slip are required to vary smoothly over the fault in order to avoid sudden, nonphysical variations in the solution. The smoothness constraint may increase the misfit value by up to 5%. The seismic moment M_0 is constrained for two reasons. First, the fault area modeled is larger than the slip area expected for a **M** 6.0 earthquake; therefore, poorly resolved areas of small slip will cause a spurious increase of M_0. Second, we are using bandpassed particle velocity; thus, we have no constraint on zero frequency. Although the GPS station distribution is not as dense as the accelerographs, the high-rate GPS could place constraints on the seismic moment. The moment constraint is only strongly enforced when the difference between model and target seismic moment is more than 15%. The target seismic moment in the inversions we present here is 9.0×10^{17} N m. We do not allow slip to occur on the edges of the modeled fault plane, which is buried 500 m below the free surface. We impose these boundary conditions by presetting slip to zero on the nodes along the edges of fault plane.

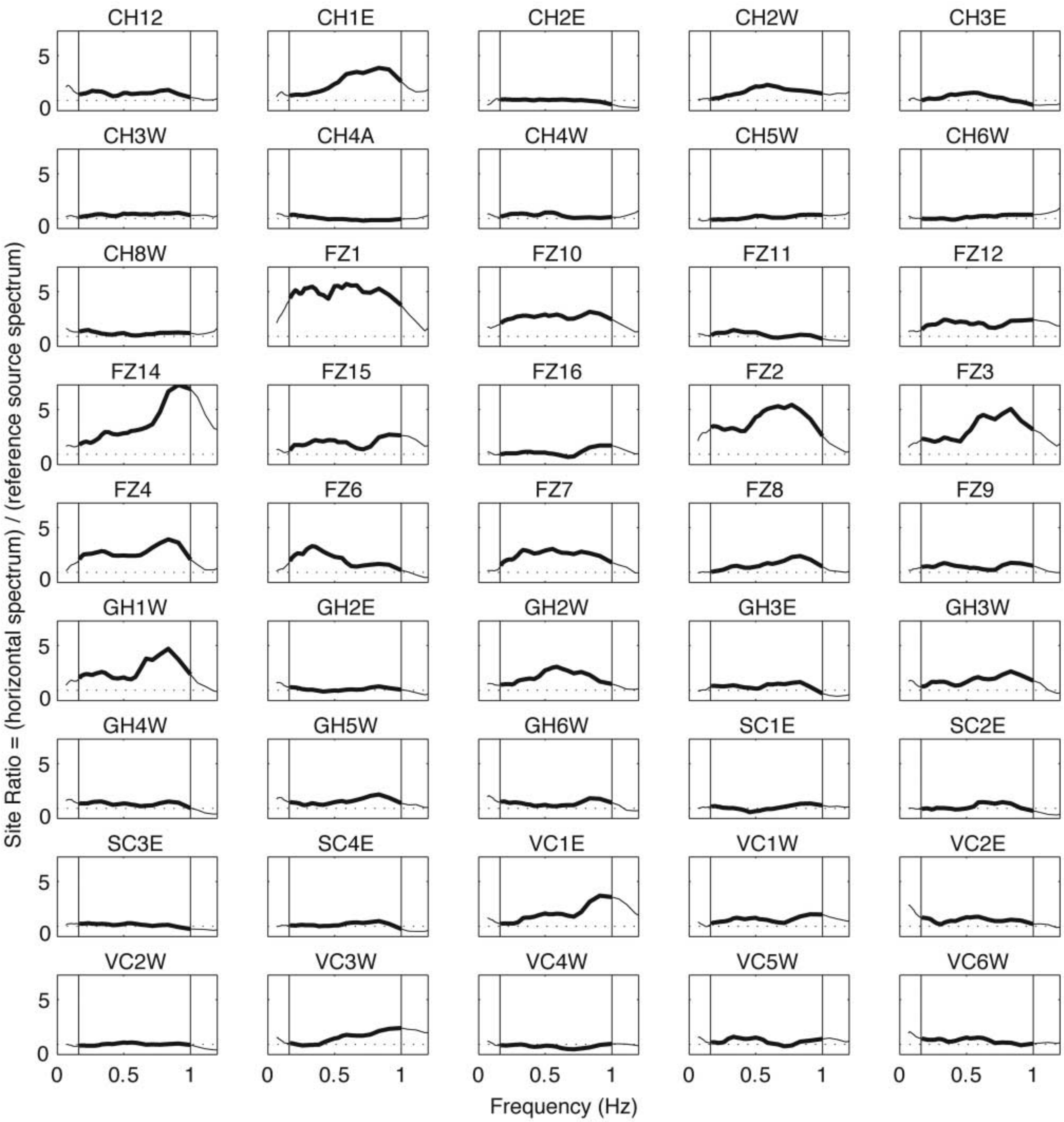

Figure 3. Site ratio for each station (horizontal spectrum divided by the source spectrum). When the horizontal spectrum equals the source spectrum, $SR = 1$ (reference horizontal dotted line), and the ground motion is not amplified. The thick line corresponds to the range 0.16 Hz $< f <$ 1.0 Hz.

We use a nonlinear simulated annealing algorithm (Liu and Archuleta, 2004) to minimize the misfit function $E(M)$ (equation 2). The need for a nonlinear inversion scheme arises from the fact that slip rake, rupture velocity, and rise time are all nonlinearly related to ground motion. The simulated annealing algorithm starts the search for a rupture model by generating a random space–time slip distribution and then perturbing that model. The perturbations are always random and have large amplitudes during the first iterations. Thus, to begin the inversion, highly dissimilar slip models are used to generate synthetics that will be compared with data. Progressively, as the slip model converges toward a final solution, the amplitude of the random variations about a preferred model decreases. As the search space narrows,

Table 2
Weights W_i and Amplification Factors A_i Attributed to CGS Stations, Based on Coalinga Earthquake Observations

Station	W_i	A_i	Station	W_i	A_i	Station	W_i	A_i	Station	W_i	A_i
C1E	0.53	1.48	FZ1	0.65	3.42	GH1W	0.56	1.79	VC1W	1.04	1.04
C2E	1.19	0.72	FZ11	0.80	0.84	GH2E	0.93	0.76	VC2E	0.79	1.07
C2W	0.68	1.12	FZ12	0.87	1.42	GH3E	1.04	0.95	VC2W	1.68	0.66
C3E	0.84	0.87	FZ15	0.76	1.31	GH3W	0.79	1.21	VC3W	0.65	0.87
C3W	2.00	0.88	FZ3	0.53	1.95	GH5W	0.87	1.04	VC4W	0.94	0.57
C4AW	0.76	0.73	FZ4	0.70	1.85				VC5W	0.78	0.87
C4W	0.89	0.88	FZ6	0.56	1.65						
			FZ7	0.71	1.69	SC1E	0.83	0.71			
			FZ8	0.72	1.01	SC2E	0.91	0.74			
			FZ9	0.86	1.04	SC3E	0.99	0.81			

The weight of vertical components in the inversion is $W_i/10$. Stations that were not installed at the time of the Coalinga earthquake were attributed $W_i = 1.5$ and $A_i = 1$ More details on the amplification factors and weights can be found in the Data section of the text.

the slip model is fine-tuned. In this procedure not all possible solutions are examined—the sets of trial source parameters considered are generated randomly and constitute a representative sample of the universe of possible solutions. The inversion procedure converges quickly to a final stable solution (Fig. 7), while assuring that the parameter space is widely covered. In other words, the final solution does not represent a local minimum of $E(M)$, but rather the best model within the proximity of the global minimum of $E(M)$.

Results

In the search for a source model, inherent nonuniqueness must be dealt with. To this end, we performed 10 inversions that use the same data and algorithm but that take different random paths. Namely, we performed 10 inversions that use different seeds for random number generation, thereby sampling different trial rupture models. The final misfits of the 10 models are small and comparable (Fig. 7). All 10 models (Fig. 8) generate synthetics waveforms that fit data equally well as indicated by the similar final values of the misfit function $E(M)$ for each model. (Ⓔ Tables 1–20, available in the electronic edition of BSSA, contain the rupture models for the 15-km-deep fault.) Figure 9 shows (A) the rupture model with the smallest final misfit; (B) the average of the 10 rupture models, (C) the standard deviation among the 10 models; and (D) the coefficient of variation (standard deviation / average).

The 10 rupture models agree in that the largest amplitude of slip (0.57 m) occurs in a small area directly southeast of the hypocenter (inside zone A, Fig. 10). A second zone of high slip is located 10 to 25 km northwest of the hypocenter, at a depth between 1 and 10 km (including zones B and C, Fig. 10). In comparing the 10 models we cannot resolve precisely the contours of this secondary zone of slip—the standard deviation goes up to 12 cm here. However, all the models point to a subdivision of this area into two patches—Zone B, about 15 km northwest of the hypocenter, at a depth of 5–9 km; and Zone C, at a depth of 2–3 km, approximately 20 km northwest of the hypocenter.

Because there is no significant slip below 10 km, and given that having a too large fault introduces error in the inversion, we also inverted the data for a fault that was only 10 km deep. Using this smaller fault, we again performed 10 inversions with different seeds for random number generation. (Ⓔ Tables 21–40, available in the electronic edition of BSSA, contain the 10 rupture models for the 10-km-deep fault.) Figure 11 shows the slip distribution and rupture-time contours obtained for the 10-km-deep fault. The main slip features identified for a 15-km-deep fault are common to the models obtained with the 10-km-deep fault. However the maximum standard deviation between the 10 models goes down to 8.7 cm when using a 10-km-deep fault.

The rupture velocity is highly heterogeneous. We compute the average rupture velocity in the two regions that present the largest slip amplitude: around the hypocenter and to the northwest of the hypocenter. These two regions, in particular the nodes over which the rupture velocity is averaged, are identified by red crosses in the model with smallest final misfit (subplot 8) in Figure 8. For those two regions—around the hypocenter and northwest of the hypocenter—the average rupture velocities over all 10 models are 2.8 km/sec and 3.3 km/sec, respectively. If we take the smallest final misfit model only, the average rupture velocities are 2.7 km/sec and 3.6 km/sec for the regions around and to the northwest of the hypocenter, respectively. The average rupture velocities in the secondary patch of slip to the northwest of the hypocenter exceeds or is very similar to (depending on the rupture model chosen) the local shear-wave velocity. The average rupture velocity is not well resolved in areas of low-amplitude slip. Small variations in the inversion parameters and inputs can alter the rupture velocity in regions of small slip by large amounts. In other inversions, not presented here, that used slightly different Green's functions (computed from slightly different velocity structures) and where the modeled fault was rotated by few degrees with

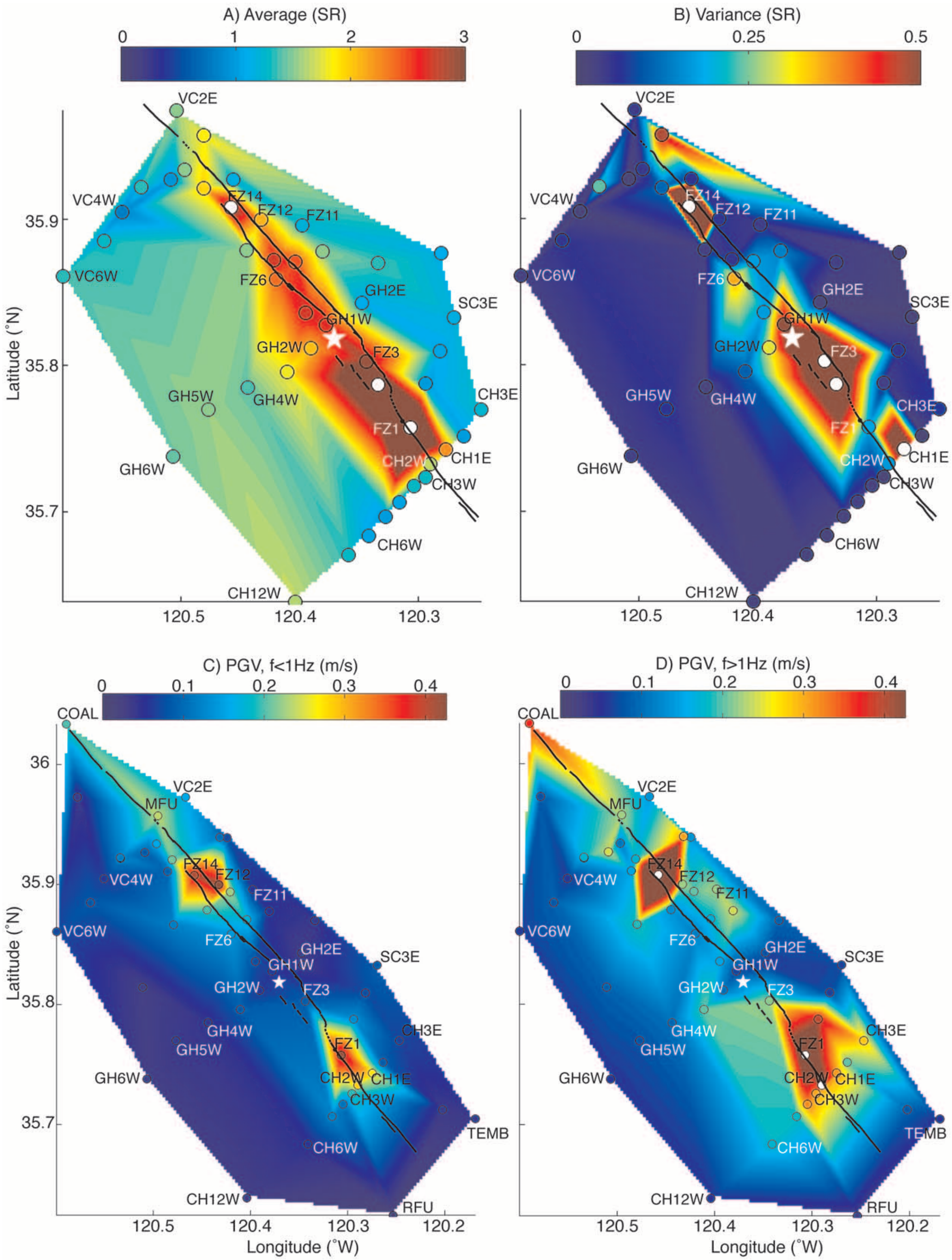

Figure 4. (A) Average of SR—local amplification. (B) Variance of SR—local resonances. (C) Peak ground velocity (PGV) at frequencies below 1 Hz, observed during the 2004 Parkfield earthquake. (D) PGV at frequencies above 1 Hz, observed during the 2004 Parkfield earthquake. All maps were produced by linear interpolation between stations. Stations represented by white circles denote values that are higher than the colorbar maximum. The white star marks the 2004 **M** 6.0 Parkfield event epicenter.

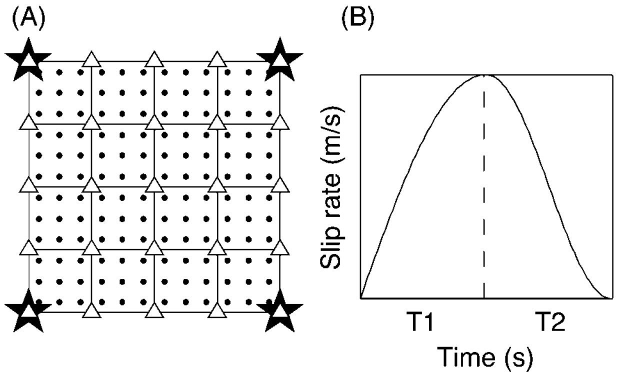

Figure 5. (A) The fault is discretized into 2 km × 2 km subfaults. Source parameters (black stars) are replaced at the corners of each subfault. Green's functions (white triangles) are computed on a finer grid (500 m × 500 m). Both source parameters and Green's function are then interpolated and convolved at a spacing of 167 m × 167 m (black dots). (B) Slip rate function $\dot{s}(t)$. The total rise time (T) is given by the sum of an accelerating rise time (T_1) and a decelerating rise time (T_2).

respect to the fault we study here, we obtained super-shear velocities along a path between the hypocenter and the top southeastern end of the fault plane. Nevertheless, if the inversions are constrained to remain subshear, models will be found that fit the data virtually as well as the super-shear models. Thus, our results indicate that no super-shear rupture speeds are required to explain the data recorded during the Parkfield mainshock.

The rake in Zone A is dominantly 180°. Zones B and C show combined right-lateral and reverse motion. We cannot resolve rise time accurately due to the narrow range of frequencies inverted (0.16 Hz $< f <$ 1.0 Hz). All 10 models yield a seismic moment of 1.08×10^{18} N m—a value that is higher than the chosen target moment.

Synthetics generated by the smallest misfit model match data very well, both in phase and amplitude (Fig. 12). As expected, most of the mismatches occur in low-amplitude seismograms, which often have lower signal-to-noise ratios, and in the vertical component. Because vertical seismograms are noisy and were downweighted by a factor of 10, they had less influence on the final rupture models. However, the number of synthetics that fit the vertical records well is quite high, indicating that our kinematic models are adequate. Most horizontal mismatches appear when one of the components, usually fault normal, is much larger than the other. There is a noticeable misfit at the station COAL, which is directly along strike. Because of the radiation pattern one would expect a null for the strike-parallel and vertical components, but this site has a strike-parallel component that is comparable to the fault normal. We have not included 3D structural effects in our inversions that could be the cause of this recording. When comparing fits between data and synthetics, one must consider the relative amplitudes of the plotted seismograms. In most cases where there are significant mismatches, the amplitudes being modeled are small.

Discussion

First, let us compare our final rupture model (Fig. 9, row B; Fig. 10A) with the following models:

1. Combined inversion of selected broadband and strong-motion waveform data, 1-sec displacement data from Global Positioning System (GPS) data and offsets determined from GPS data, using the method of Ji *et al.* (2002) (Bakun *et al.*, 2005)
2. Combined inversion of static GPS and InSAR data (Johanson *et al.*, 2006)
3. Inversion of GPS static data (Murray and Langbein, 2006)
4. Inversion of continuous high-rate GPS data (Johnson *et al.*, 2006)

Zone A (Fig. 10A) appears in Models 1 and 2—although there is no agreement for the value of maximum slip in Zone A, there is agreement on the shape, size and location of the zone. Due to the geometry of the geodetic network, Model 3 would not be able to resolve slip in a small deep region around the hypocenter (Langbein *et al.*, 2006; J. R. Murray, personal comm., 2006; Murray and Langbein, 2006). Given that Model 4 is obtained from data recorded at the same stations as the ones used to derive Model 3, Model 4 may have the same limitations as Model 3 due to the geometry of the GPS network. Zone B is present in all of the above models—our rupture model is in very good agreement with all the above models in terms of the shape, area, and maximum slip in this region. Our standard deviation reaches its maximum value here, indicating that strong-motion data cannot accurately resolve the contours of slip in Zone B. Custódio *et al.* (2005) obtained a similar result. After inverting multiple subsets of strong-motion data from the Parkfield earthquake, the slip distribution towards the northwest end of the fault remained undefined. Very high peak ground accelerations (Shakal *et al.*, 2006), including one station that recorded 2.5*g* (Shakal and Haddadi, 2006), were observed toward the northwest of the hypocenter. Also, surface afterslip attained its maximum values northwest of the hypocenter (Lienkaemper *et al.*, 2006; Rymer *et al.*, 2006). Both observations are consistent with a large amplitude of shallow slip in Zone C. Region C is absent from all the independent models above.

Table 3
Range of Source Parameters Searched in the Kinematic Inversion

Source Parameter	Lower Limit	Upper Limit
Slip amplitude (m)	0	1.0
Slip rake (°)	120	180
Rupture velocity (km/sec)	2.0	5.0
Rise time (sec)	0.2	2.0

Table 4
The Two One-Dimensional Velocity Structures Used in the Computation of Green's Functions

Southwest						Northeast					
Thickness (km)	Density (kg/m^3)	V_P (km/sec)	V_S (km/sec)	Q_P	Q_S	Thickness (km)	Density (kg/m^3)	V_P (km/sec)	V_S (km/sec)	Q_P	Q_S
1.0	2000	1.9	1.0	70	35	0.7	2000	2.0	1.1	70	35
1.0	2300	3.4	1.7	270	160	0.7	2300	3.8	2.2	300	180
1.0	2300	4.6	2.4	450	260	0.6	2300	4.3	2.4	340	190
1.0	2700	5.1	3.1	500	300	1.6	2300	4.8	2.7	450	250
1.4	2700	5.6	3.6	550	350	4.0	2500	5.3	3.1	500	300
13.3	2800	6.3	3.6	600	350	6.7	2700	5.8	3.3	550	300
∞	2800	6.8	3.6	680	360	6.2	2800	6.2	3.8	600	350
						4.1	2800	6.8	3.8	650	350
						∞	2800	7.0	4.0	700	400

The table shows, for each side of the fault, layer thickness, density (ρ), P-wave velocity (V_P), S-wave velocity (V_S), and P- and S-wave attenuation ($1/Q_P$ and $1/Q_S$, respectively). The P-wave structure is obtained by interpolation of the 3D model of *Thurber et al.* (2006). The S-wave structure is obtained by applying a 1D bilateral interpolation of the V_P/V_S ratio of *Thurber et al.* (2003) to the previously derived 1D P-wave structure. Finally, the 1D model is adapted so that the layers are common to the P- and S-wave structures. This last step speeds up the computation of the Green's functions.

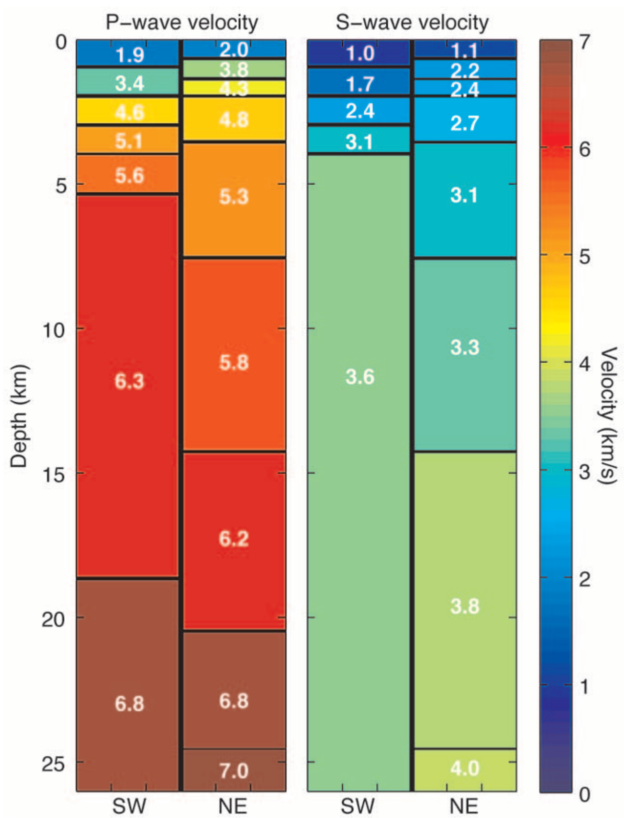

Figure 6. 1D velocity structure derived from the 3D models of Thurber *et al.* (2006) and Thurber *et al.* (2003). See footnote of Table 4 for details.

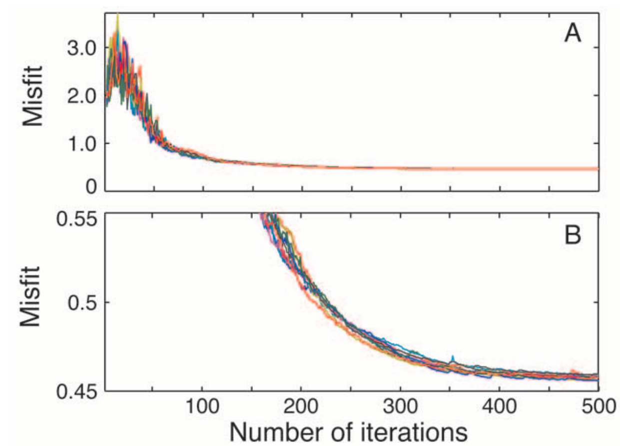

Figure 7. Misfit vs. iteration step for 10 rupture models: (A) complete misfit range; (B) zoom in at $0.45 < E(M) < 0.55$. The 10 models were computed using the same data and algorithm, but different seeds for random number generation. The inversions evolve quickly toward a stable solution.

Because the rupture velocity is highly heterogeneous, with some regions of the fault not well resolved, we cannot confidently provide an average velocity. Considering all 10 models presented here, the average rupture velocity from the hypocenter to a given point on the fault is ~2.8 km/sec for nodes in the hypocentral region and ~3.3 km/sec for nodes to the northwest of the hypocenter (Fig. 8). The slow rupture velocities, toward the northwest at very shallow depths, obtained in all our 10 models, may be the reason why no surface rupture occurred in spite of a large shallow slip in this region. The rupture velocity estimated by the U.S. Geological Survey Parkfield Dense Seismograph Array (UPSAR) is very heterogeneous over the fault plane without reaching super-shear values (Fletcher *et al.*, 2006). We find that super-shear rupture speeds are not required to explain the strong-motion data, despite having obtained average rupture velocities that are super-shear in some of our models (including unpublished results).

Models 2, 3, and 4 assume pure right-lateral slip; Model 1 allows the rake to change over the fault. Model 1, like our model, shows approximate horizontal motion close to the

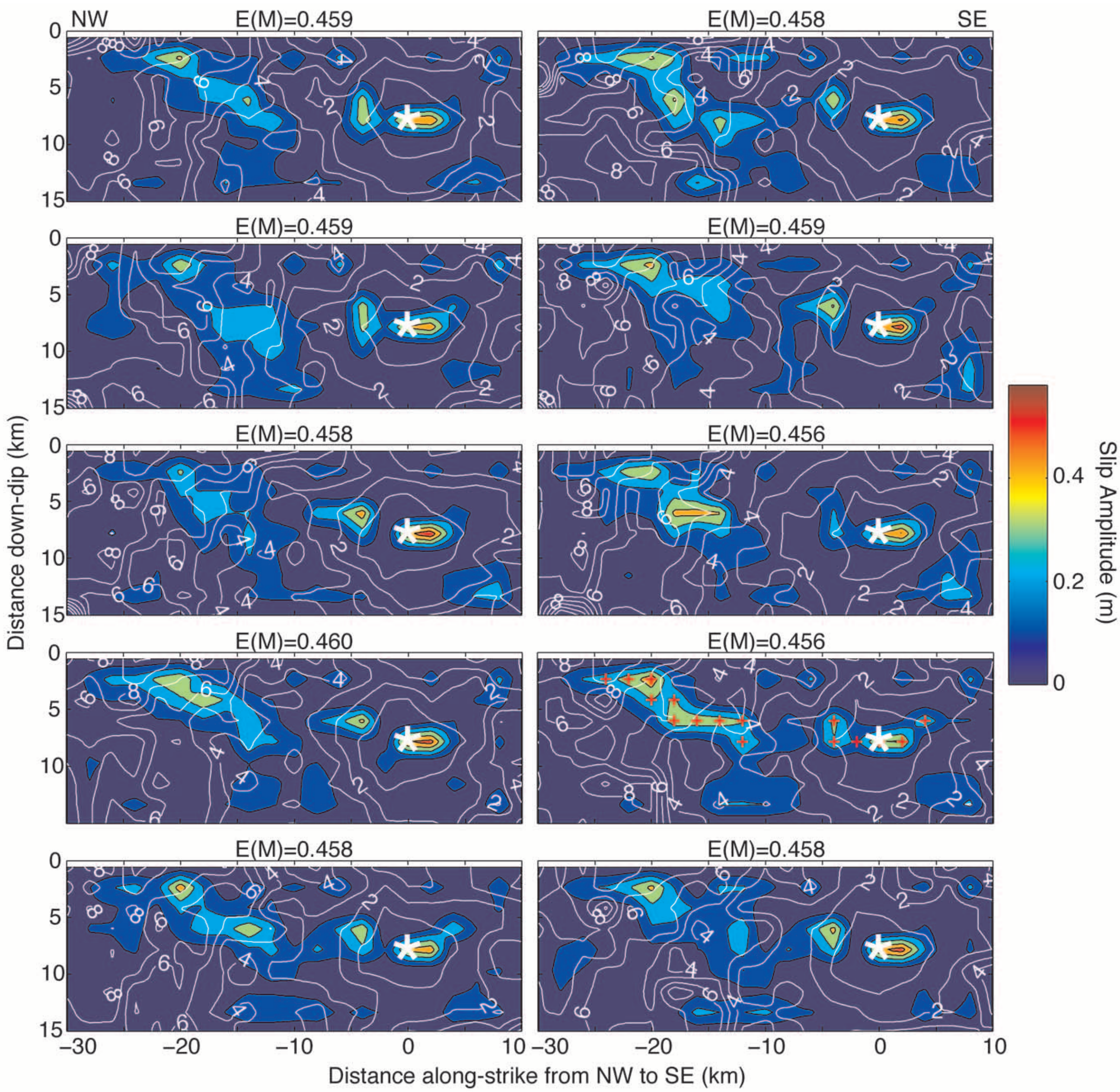

Figure 8. Ten rupture models obtained by inversion of strong-motion, near-source velocity waveforms. The 10 models were computed using the same data and algorithm but different seeds for random number generation. The color contours show slip amplitude (*m*). The white contours show rupture time in 1-sec contours. The white asterisk marks the hypocenter. The misfit of each model is indicated above each slip distribution. Rupture velocity averaged in the hypocentral region and in the region of slip to the northwest of the hypocenter is ~2.7 km/sec and ~3.6 km/sec, respectively, for the model with the smallest misfit. The red crosses mark the nodes over which the rupture velocity was averaged. The rupture velocity averaged over the 10 models is ~2.8 km/sec in the hypocentral region and ~3.3 km/sec in the region of high slip to the northwest of the hypocenter. The rupture velocity is highly heterogeneous.

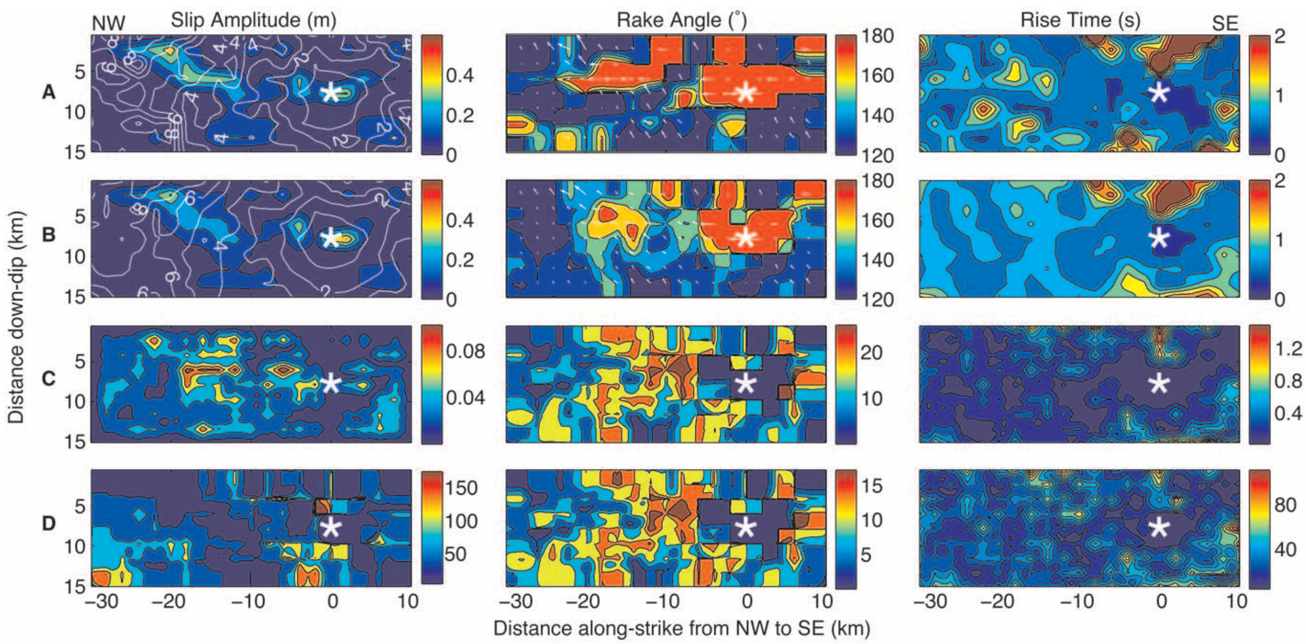

Figure 9. Source parameters. First column: slip amplitude (m) and rupture time (white lines are 1-sec contours); second column: rake angle (°) and slip vector field (white arrows); third column: rise time (sec). (A) Rupture model with smallest final misfit; (B) average of 10 models; (C) standard deviation between the 10 models; and (D) coefficient of variation. The average retains only the coherent features from the 10 models obtained with different random seeds. The standard deviation measures the difference between the average and each of the 10 individual models. The coefficient of variance shows the percentage of variability of individual models with respect to the average. The coefficient of variation is maximum in areas with a small amount of slip, where the slip value is not well resolved. The white asterisk marks the hypocenter.

hypocenter, but toward the northwest the rake angle tends toward 90° at shallow depth as expected (Chinnery, 1961). Models 1, 2, and 3 yield seismic moments of 9.4×10^{17} N m. 2.43×10^{18} N m, and 1.3×10^{18} N m respectively. We obtain M_0 of 1.08×10^{18} N m—this is a constrained value.

In Figure 10, we show our final slip distribution, relocated seismicity from 1984 to 2004 and cross sections of P-wave velocity parallel to the San Andreas Fault (SAF) (Thurber *et al.*, 2006). Individual regions of the fault behave in different manners:

- The greatest amplitude of slip occurred in Zone A, primarily in a small area around the hypocenter. The largest aftershocks in the hypocentral region took place on the edges of Zone A. The level of seismic activity in Zone A before the mainshock is low. The hypocenter is located on the southeast edge of a relatively high P-wave velocity body that exists on the northeast side of the fault. Curiously, the 1966 Parkfield earthquake hypocenter is located on the northwest edge of the same high-velocity body.
- Zones B and C, which slipped during the mainshock, were relatively free of aftershocks. As noted by Thurber *et al.* (2006), most aftershocks overlap previous microseismicity.
- Zone B includes regions that slipped in 1993 and 1994 in **M** 4.5 and **M** 5 earthquakes.
- Zone C, the region of the fault that has the largest amplitude of slip after the hypocenter, is sandwiched between two bodies of relatively high wave speed on the southwest side of the fault.
- One of the two **M** 5 aftershocks coincided with the 1993 **M** 5 hypocenter, in Zone D.
- Zone F is delineated by several small aftershocks. In our model, this zone shows no evidence of coseismic slip. This region is on the top edge of the high-velocity body present on the northeast side of the San Andreas Fault.

Earlier studies suggested that areas of high-velocity correlated positively to zones of high dynamic slip and vice-versa (Nicholson and Lees, 1992; Lees and Nicholson, 1993). The same studies furthermore indicated that large earthquakes nucleated in regions of strong gradients in the velocity structure. We find no obvious correlation between slip distribution and material velocity. However, the **M** 6.0 Parkfield earthquakes seem to have nucleated in the edges of a high-velocity body on the northeast side of the fault.

The large peak ground velocities (PGVs) observed during this **M** 6.0 earthquake can be explained in part by site effects (Fig. 4). Strong amplifications and resonances affect the stations that registered high PGVs below 1 Hz (FZ12, FZ14, FZ1, CH1E, and CH2W). After correcting for site effects (see earlier discussion of how this was done), the

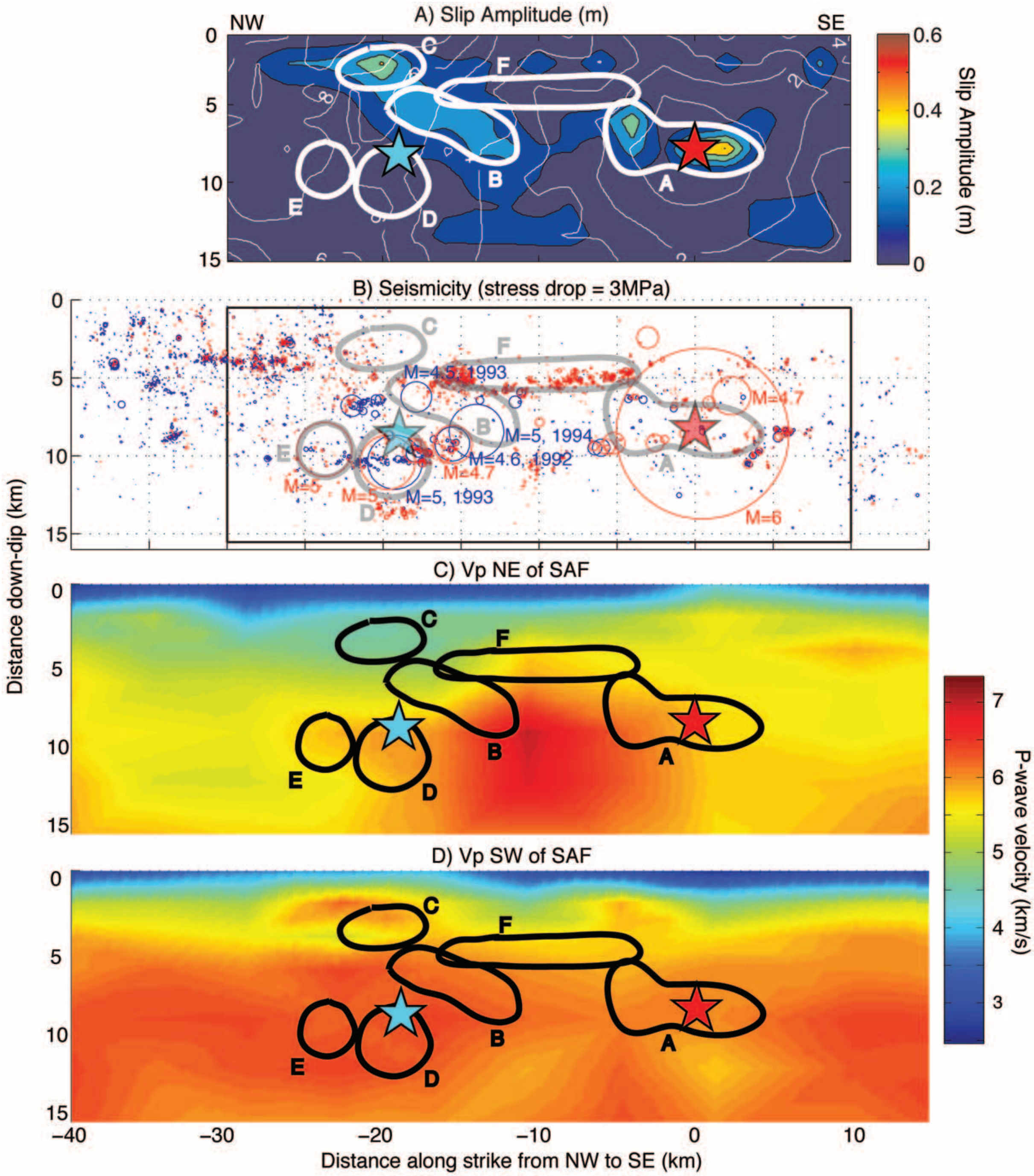

Figure 10. (A) Slip distribution and 1-sec rupture time contours for the average model (model obtained by averaging the 10 best models). (B) Seismicity before (blue) and after (red) the 2004 mainshock (1984–2004) (Thurber *et al.*, 2006). The size computed for the earthquakes assumes a circular rupture area and a constant stress drop of 3 MPa. Earthquakes greater than **M** 4.5 are labeled with their magnitude and if they happened before the 2004 mainshock, with the year of their occurrence. (C) *P*-wave velocity on the northeast side of the fault zone (Thurber *et al.*, 2006). (D) *P*-wave velocity on the southwest side of the fault zone (Thurber *et al.*, 2006). For more details on the velocity structure see Thurber *et al.* (2006). The red and blue stars mark the 2004 and 1966 **M** 6 hypocenters, respectively.

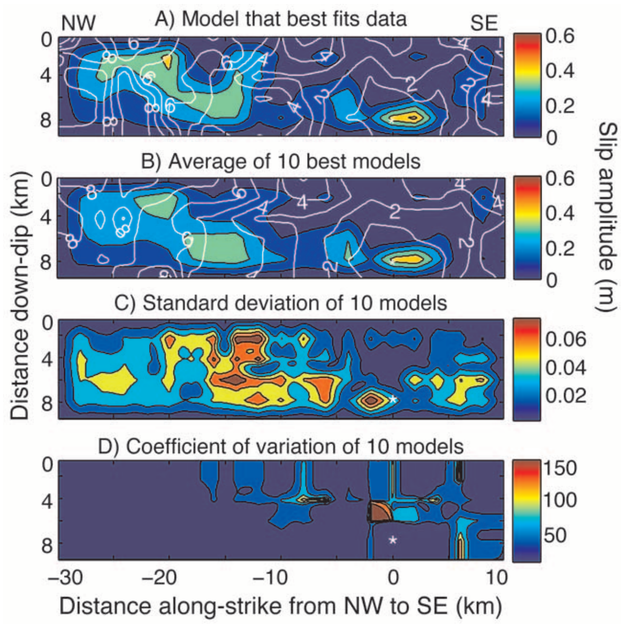

Figure 11. Rupture model obtained using a 10-km-deep fault. The color contours show slip amplitude (m), and the white lines indicate the rupture time in 1-sec intervals. (A) Rupture model with smallest final misfit; (B) average of 10 models; (C) standard deviation between the 10 models; and (D) coefficient of variation derived from the 10 models. The white asterisk marks the hypocenter. See caption of Figure 9 and text for details on the different plots.

ground motion at these stations was well replicated by the synthetic ground motion generated by our kinematic rupture model.

The large amount of data tightly constrains the inversion. However, the Parkfield seismic data is noisy in the sense that at many stations the source signal is strongly masked by effects for which we cannot perfectly correct (e.g., 3D velocity structure, unaccounted site effects, etc.). Within these limitations, our rupture model generates synthetic ground motion that agrees closely with the data, even when the data were not highly weighted in the inversion.

Conclusions

We have inverted ground velocity records of the 2004 **M** 6.0 Parkfield earthquake from 43 near-source accelerographs. We approximate the velocity structure as two different layered half-spaces separated by the fault. Using the records from the 1983 Coalinga earthquake we were able to assess the effects of local site conditions. Using a weighting scheme that reflected the site effects and after correcting the data for local amplifications, we inverted the particle velocity seismograms using the nonlinear method of Liu and Archuleta (2004). We find that the hypocentral region (Zone A, Fig. 10) produced the maximum amplitude of slip in a pure right-lateral sense. A secondary more extensive region to the northwest of the hypocenter (Zones B and C) also ruptured. Details of slip cannot be resolved in this region. After nucleating in a relatively quiet seismic region (Zone A) and breaking through Zone B, the rupture continued to shallower depths, into Zone C. Zones A, B and C are all characterized by low-level background seismicity. The rupture did not proceed into the Zones D and E, which produced **M** 5.0 aftershocks in the two days following the mainshock. Our model yields a maximum slip amplitude of 0.57 m and high average rupture velocities of ~2.8 km/sec and ~3.3 km/sec in the regions of high slip, where the rupture velocity is best resolved. Even though our time-space slip models show a zone of shallow slip towards the northwest of the hypocenter, no surface break occurred at the time of the mainshock. This may be related to the slow rupture velocities in the northwest zone of very shallow slip. This zone where we infer shallow slip is near the region where the largest amount of afterslip (Rymer *et al.*, 2006) and highest PGAs (Shakal *et al.*, 2006; Shakal and Haddadi, 2006) were observed. The distribution and high values of the observed PGVs can be partly explained by site effects.

Acknowledgments

Data used in this study were collected, preprocessed, and made available by the California Geological Survey (CGS) and the United States Geological Survey (USGS). A cluster sponsored by Hewlett-Packard at the California NanoSystems Institute (CNSI), UC Santa Barbara, was used for the computations. S. Custódio acknowledges a Ph.D. fellowship from *Fundação para a Ciência e Tecnologia* (Portuguese Foundation for Science and Technology). This work was supported by a grant from the National Science Foundation EAR-0512000 and by a grant from the Southern California Earthquake Center (SCEC). SCEC is funded by NSF Cooperative Agreement EAR-0106924 and USGS Cooperative Agreement 02HQAG0008. The SCEC Contribution Number for this article is 929. This is Institute for Crustal Studies (ICS) Contribution Number 0696.

References

Bakun, W. H., and A. G. Lindh (1985). The Parkfield, California, earthquake prediction experiment, *Science* ***229,*** 619–624.

Bakun, W. H., and T. V. McEvilly (1984). Recurrence models and Parkfield, California, earthquakes, *J. Geophys. Res.* **87,** no.18, 3051–3058, doi 10.1029/0JGREA0000890000B5003051000001.

Bakun, W. H., B. Aagaard, B. Dost, W. L. Ellsworth, J. L. Hardebeck, R. A. Harris, C. Ji, M. J. S. Johnston, J. Langbein, J. J. Lienkaemper, A. J. Michael, J. R. Murray, R. M. Nadeau, P. A. Reasenberg, M. S. Reichle, E. A. Roeloffs, A. Shakal, R. W. Simpson, and F. Waldhauser (2005), Implications for prediction and hazard assessment from the 2004 Parkfield earthquake, *Nature* **437,** 969–974.

Ben-Zion, Y., J. R. Rice, and R. Dmowska (1993). Interaction of the San Andreas fault creeping segment with adjacent great rupture zones and earthquake recurrence at Parkfield, *J. Geophys. Res.* **98,** 2135–2144.

Borcherdt, R. D., M. J. S. Johnston, C. Dietel, G. Glassmoyer, D. Myren, and C. Stephens (2004). Acceleration and volumetric strain generated by the Parkfield 2004 earthquake on the GEOS strong-motion array near Parkfield, California, *U.S. Geol. Surv. Open-File Rep. 2004-1376.*

Chinnery, M. A. (1961). The deformation of the ground around surface faults, *Bull. Seism. Soc. Am.* ***51,*** no. 3, 355–372.

Custódio, S., P. Liu, and R. J. Archuleta (2005). The 2004 M_w 6.0 Parkfield, California, earthquake: inversion of near-source ground motion using multiple data sets. *Geophys. Res. Let.* **32,** L23-312, doi 10.1029/2005GL024417.

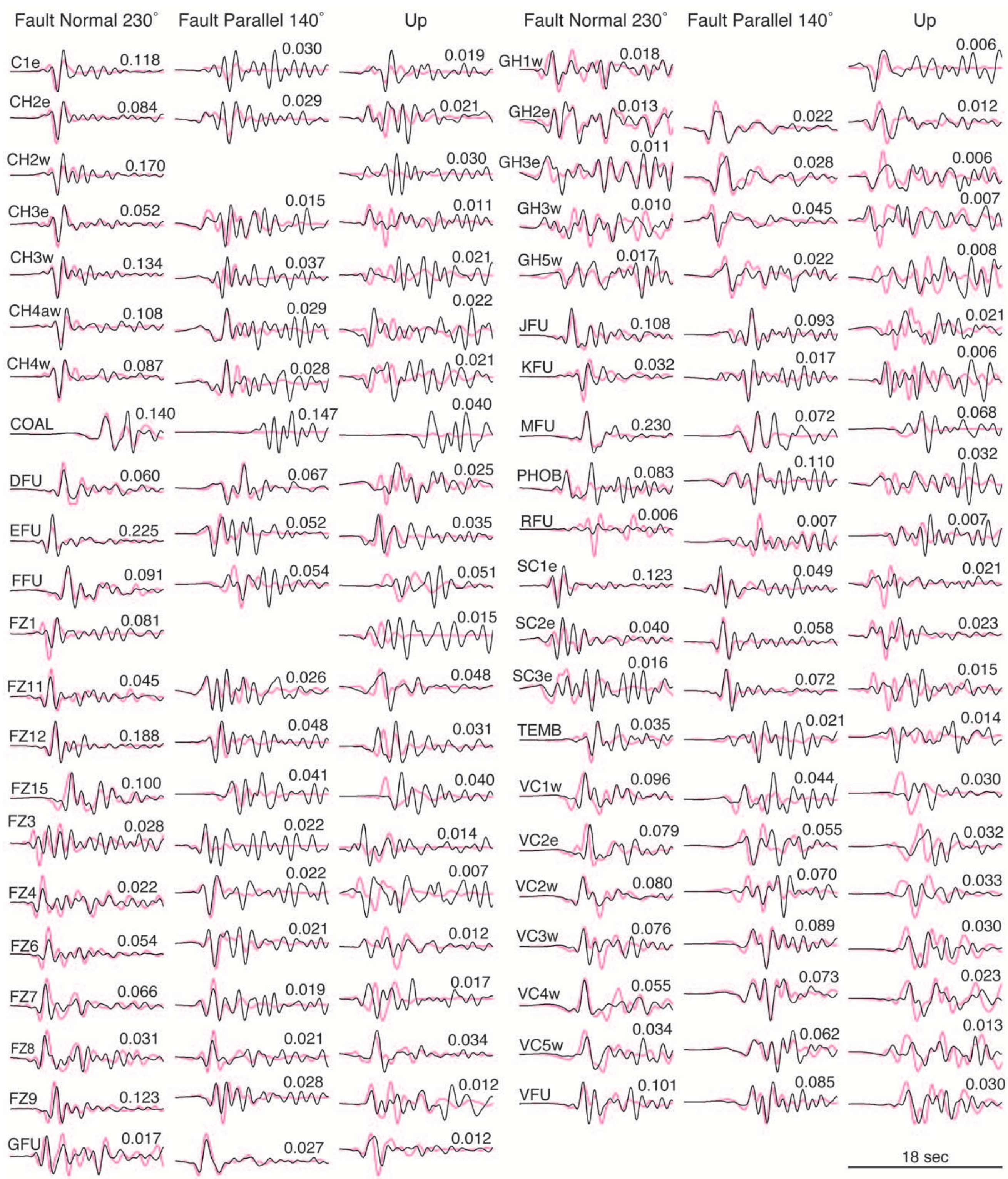

Figure 12. Comparison between inverted data $\dot{u}_o(t)/A_i$ (black) and synthetics $\dot{u}_s(t)$ (red) generated by the model with smallest final misfit (15-km-deep fault). The components of motion shown are fault normal (230° clockwise from north), fault parallel (140° clockwise from north) and vertical (up). The codes of the stations are indicated at the beginning of each row. All waveforms are normalized. The peak velocity (m/sec) of each inverted seismogram is indicated on its top right corner. The total length of the waveforms is 18 sec.

Eberhart-Phillips, D. (1989). Active faulting and deformation of the Coalinga anticline as interpreted from three-dimensional velocity structure and seismicity, *J. Geophys. Res.* **94,** no. 13, 15,565–15,586, doi 10.1029/89JB01390.

Eberhart-Phillips, D., and A. J. Michael (1993). Three-dimensional velocity structure, seismicity, and fault structure in the Parkfield Region, central California, *J. Geophys. Res.* **98,** 15,737–15,758.

Fletcher, J. B., and P. Spudich (1998). Rupture characteristics of the three $M \approx 4.7$ (1992-1994) Parkfield earthquakes, *J. Geophys. Res.* **103,** 835–854, doi 10.1029/97JB01797.

Fletcher, J. B., P. Spudich, and L. M. Baker (2006). Direct observation of earthquake rupture propagation in the 2004 Parkfield, California, earthquake using the UPSAR accelerograph array, *Bull. Seism. Soc. Am.* **96,** no. 4B, S129–S142.

Harris, R. A., and P. Segall (1987). Detection of a locked zone at depth on the Parkfield, California, segment of the San Andreas fault, *J. Geophys. Res.* **92,** 7945–7962.

Ji, C., D. J. Wald, and D. V. Helmberger (2002). Source description of the 1999 Hector Mine, California, earthquake, part I: wavelet domain inversion theory and resolution analysis, *Bull. Seism. Soc. Am.* **92**, no. 4, 1192–1207.

Johanson, I. A., E. J. Fielding, F. Rolandone, and R. Bürgmann (2006). Coseismic and postseismic slip of the 2004 Parkfield earthquake from space-geodetic data, *Bull. Seism. Soc. Am.* **96,** no. 4B, S269–S282.

Johnson, K. M., R. Bürgmann, and K. Larson (2006). Frictional afterslip following the 2004 Parkfield, California, earthquake, *Bull. Seism. Soc. Am.* **96,** no. 4b, S321–S338.

Kilb, D., G. Biasi, J. Brune, J. Anderson, and F. L. Vernon (2003). Quantifying properties of seismic spectra: an examination of 100's of spectra from southern California earthquakes recorded by the ANZA seismic network, *EOS Trans. AGU* **84,** no. 46, Fall Meet. Suppl., S42C-0173 (abstract).

Langbein, J., R. Borcherdt, D. Dreger, J. Fletcher, J. L. Hardebeck, M. Hellweg, C. Ji, M. Johnston, J. R. Murray, and R. Nadeau (2005). Preliminary report on the 28 September 2004, M 6.0 Parkfield, California earthquake, *Seism. Res. Lett.* **76,** 10–26.

Langbein, J., J. R. Murray, and H. A. Snyder (2006). Coseismic and initial postseismic deformation from the 2004 Parkfield, California, earthquake observed by Global Positioning System, creepmeters, and borehole strainmeters. *Bull. Seism. Soc. Am.* **96,** no. 4B, S304–S320.

Lees, J. M., and C. Nicholson (1993). Three-dimensional tomography of the 1992 Southern California earthquake sequence; constraints on dynamic earthquake rupture? *Geology* **21,** no. 5, 387–390.

Li, Y., P. Leary, K. Aki, and P. Malin (1990). Seismic trapped modes in the Oroville and San Andreas fault zones, *Science* **249,** 763–766.

Li, Y., J. E. Vidale, and E. S. Cochran (2004). Low-velocity damaged structure of the San Andreas Fault at Parkfield from fault zone trapped waves, *Geophys. Res. Lett.* **31,** L12S06, doi 10.1029/2003GL019044.

Lienkaemper, J. J., B. Baker, and F. S. McFarland (2006). Surface slip associated with the 2004 Parkfield, California, earthquake measured on alinement arrays, *Bull. Seism. Soc. Am.* **96,** no. 4B, S239–S249.

Liu, P., and R. J. Archuleta (2004). A new nonlinear finite fault inversion with three-dimensional Green's functions: application to the 1989 Loma Prieta, California, earthquake, *J. Geophys. Res.* **109,** BO2318 doi 10.1029/2003JB002625.

Malin, P. E., and M. G. Alvarez (1992). Stress diffusion along the San Andreas fault at Parkfield, California, *Science* ***256,*** 1005–1007.

McJunkin, R. D., and A. F. Shakal (1983). Parkfield strong-motion array, *Calif. Geol.* **36,** 27–34.

Michelini, A., and T. V. McEvilly (1991). Seismological studies at Parkfield, part I: Simultaneous inversion for velocity structure and hypocenters using cubic B-splines parameterization, *Bull. Seism. Soc. Am.* **81,** no. 2, 524–552.

Murray, J., and J. Langbein (2006). Slip on the San Andreas Fault at Parkfield, California, over two earthquake cycles and the implications for seismic hazard, *Bull. Seism. Soc. Am.* **96,** no. 4B, S283–S303.

Murray, J. R., P. Segall, P. Cervelli, W. Prescott, and J. Svarc (2001). Inversion of GPS data for spatially variable slip-rate on the San Andreas Fault near Parkfield, CA, *Geophys. Res. Lett.* ***28,*** 359–362, doi 10.1029/2000GL011933.

Nicholson, C., and J. M. Lees (1992). Travel-time tomography in the northern Coachella Valley using aftershocks of the 1986 ML 5.9 North Palm Springs earthquake, *Geophys. Res. Let.* **19,** 1–4.

Roeloffs, E., and J. Langbein (1994). The earthquake prediction experiment at Parkfield, California, *Rev. Geophys.* **32,** 315–336.

Rymer, M. J., J. C. Tinsley, J. A. Treiman, J. R. Arrowsmith, K. B. Clahan, A. M. Rosinski, W. A. Bryant, H. A. Snyder, G. S. Fuis, N. Toké, and G. W. Bawden (2006). Surface fault afterslip associated with the 2004 Parkfield, California, earthquake, *Bull. Seism. Soc. Am.* **96,** no. 4B, S11–S27.

Segall, P., and Y. Du (1993). How similar were the 1934 and 1966 Parkfield earthquakes? *J. Geophys. Res.* ***98,*** 4527–4538.

Shakal, A., and H. Haddadi (2006). Note on the interpretation and reconstruction of the very high acceleration fault zone 16 station record from the 2004 Parkfield earthquake. *Bull. Seism. Soc. Am.* **96,** no. 4B, S119–S128.

Shakal, A., H. Haddadi, V. Graizer, K. Lin, and M. Huang (2006). Some key features of the strong-motion data from the **M** 6.0 Parkfield, California, earthquake of 28 September 2004, *Bull. Seism. Soc. Am.* **96,** no. 4B, S90–S118.

Spudich, P., and D. P. Miller (1990). Seismic site effects and the spatial interpolation of earthquake seismograms: results using aftershocks of the 1986 North Palm Springs, California, earthquake, *Bull. Seism. Soc. Am.* **80,** no. 6, 1504–1532.

Thurber, C., S. Roecker, K. Roberts, M. Gold, L. Powell, and K. Rittger (2003). Earthquake locations and three-dimensional fault zone structure along the creeping section of the San Andreas fault near Parkfield, CA: preparing for SAFOD, *Geophys. Res. Lett.* **30,** 1112, doi 10.1029/2002GL016004.

Thurber, C., H. Zhang, F. Waldhauser, J. Hardebeck, A. Michael, and D. Eberhart-Phillips (2006). Three-dimensional compressional wavespeed model, earthquake relocations, and focal mechanisms for the Parkfield, California, region, *Bull. Seism. Soc. Am.* **96,** no. 4B, S38–S49.

Unsworth, M., and P. A. Bedrosian (2004). Electrical resistivity structure at the SAFOD site from magnetotelluric exploration, *Geophys. Res. Lett.* no. 31, 12, L12S05. doi 10.1029/2003GL019405.

Waldhauser, F., W. L. Ellsworth, D. P. Schaff, and A. Cole (2004). Streaks, multiplets, and holes: high-resolution spatio-temporal behavior of Parkfield seismicity, *Geophys. Res. Lett.* **31,** no. 18, L18,608, doi 10.1029/0JGREA0000890000B5003051000001.

Wallace, R. E. (1990). The San Andreas fault system, California, *U.S. Geol. Surv. Prof. Paper 1515.*

Zhu, L., and L. A. Rivera (2002). A note on the dynamic and static displacements from a point source in multilayered media, *Geophys. J. Int.* **148,** 619–627, doi 10.1046/j.1365246X.2002.01610.x.

Institute for Crustal Studies
Girvetz Hall
University of California
Santa Barbara, California 93106
pcliu@crustal.ucsb.edu
susana@crustal.ucsb.edu
ralph@crustal.ucsb.edu
(P.L., S.C., R.J.A.)

Department of Earth Science
Webb Hall
University of California
Santa Barbara, California 93106
(S.C., R.J.A.)

Manuscript received 27 September 2005.